

## AERO-THERMAL-ELASTICITY-MATERIALS OPTIMIZATION OF COOLED GAS TURBINE BLADES: PART II

**G. S. Dulikravich\***, **T. J. Martin\*\***, **B. H. Dennis\*\*\*** and **I. N. Egorov\*\*\*\***

\* Department of Mechanical and Materials Engineering, Florida International University,  
MAIDROC Laboratory, 10555 W. Flagler St., Miami, FL 33174, U.S.A.

\*\* Pratt & Whitney Engine Company, Turbine Discipline Engineering & Optimization Group,  
M/S 169-20, East Hartford, CT 06108, U.S.A.

\*\*\* Department of Mechanical and Aerospace Engineering, University of Texas at Arlington,  
UTA Box 19018, 500 West First Street, Arlington, TX 76019, U.S.A.

\*\*\*\* IOSO Technology Center, Vekovaia St., 21, Office 203, 109544, Moscow, Russia

### ABSTRACT

The first lecture in this two-lecture sequence provides background and general concepts. This second lecture provides practical optimization examples. The objective of these two lectures is to provide a modular design optimization tool description that will take into account interaction of the hot gas flow-field, heat transfer in the blade material, internal coolant flow-field, and stresses and deformations in a multi-stage axial gas turbine blade.

### 1. Quasi 3-D conjugate aero-thermal optimization of coolant passages

A preliminary design optimization tool has been developed [1-4] for quasi 3-D conjugate aero-thermal optimization of internally cooled turbine blades with or without thermal barrier coating and no film cooling. A 3-D heat conduction analysis, using the boundary element method (BEM), was iteratively coupled to an unstructured finite volume Reynolds-averaged Navier-Stokes CFD analysis for turbulent hot gas flow in 2-D blade-to-blade surfaces. A quasi-one-dimensional system with heat addition and friction was iteratively coupled to the BEM heat conduction via heat flux for the simulation of the airflow in the serpentine coolant passages. Lessons learned from this effort lead to the question, *“Can we design a turbine cooling scheme that simultaneously increases the turbine inlet temperature and decreases the required coolant mass flow rate with a constraint of keeping the maximum temperature of the blade material below a specified limit?”*

Unfortunately, both of these quantities were used as design variables in our coolant flow passage optimization procedure that utilized an older version of a hybrid optimizer [5]. For this reason, they could not be extremized explicitly. Therefore, several alternative objectives were formulated. The uniform temperature objective was effective at reducing the temperature gradients in the blade, but it did not always produce effective coolant flow passage designs.

Extremization of the integrated heat flux into the blade produced only the trivial results of reducing the sizes of the coolant passages (minimum integrated heat flux), or by making the coolant walls as thin as possible (maximum integrated heat flux).

The minimization of the coolant temperature at the ejection point, while enforcing the maximum temperature equality constraint, was successful. It decreased the required coolant mass flow rate and the required coolant heat transfer coefficients (thus coolant passage surface roughness and coolant pressure losses) for the test cases that were studied, while keeping the turbine inlet temperature almost unchanged.

But, when the minimization of the coolant temperature at the ejection point was performed while enforcing the maximum temperature inequality constraint, the results were unacceptable. Although the required coolant mass flow rate reduced significantly, the turbine inlet temperature also decreased significantly. Besides, the walls and the struts of the resulting blade were unacceptably thin (Fig. 1b).

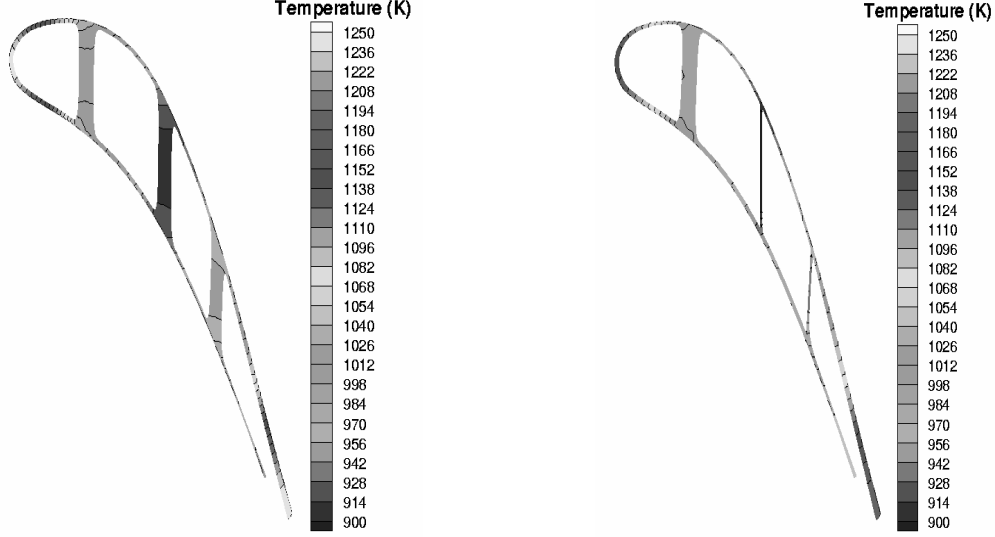


Figure 1: Optimized blade interior geometries and temperatures for minimized coolant ejection temperature design of an internally cooled turbine blade using; a) the maximum temperature equality constraint, and b) the maximum temperature inequality constraint.

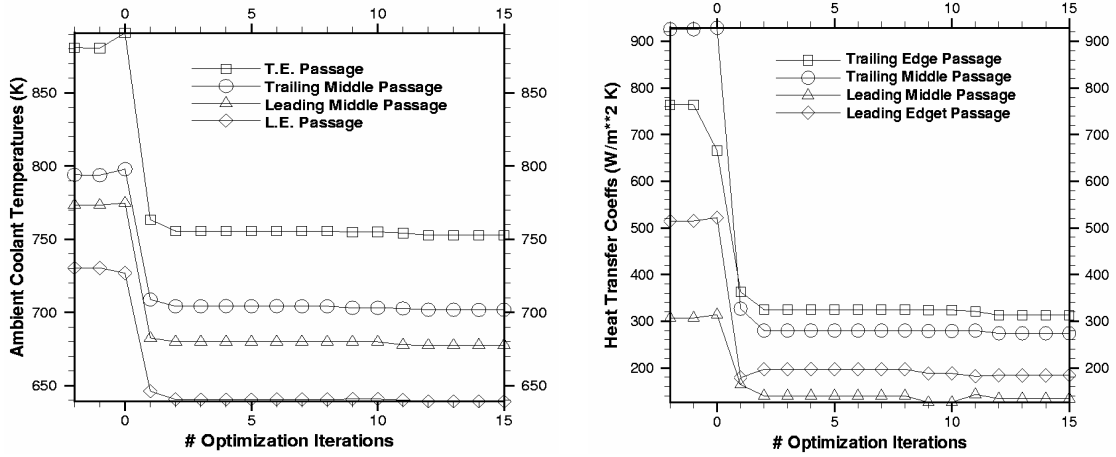


Figure 2: Evolution of optimum bulk coolant temperatures (left) and the coolant passage wall heat transfer coefficients (right) in each of the four coolant flow passages for the minimization of coolant ejection temperature when using the maximum temperature equality constraint.

Specifically, two different minimizations of the coolant ejection temperature were performed; one with the maximum temperature equality constraint,  $T_{\max} = \overline{T_{\max}}$ , and the other with the inequality constraint  $T_{\max} < \overline{T_{\max}}$ . The design sensitivity gradients were calculated using finite differencing and the optimization program was initiated with the DFP. The optimization with the equality constraint required 15 cycles and 794 objective function evaluations. The large number of function evaluations was needed because forward finite differencing was used to obtain the sensitivity gradients. After four optimization cycles, the

program switched to the GA, switching finally to the NM in the 14th cycle. Results of this quasi-conjugate heat transfer optimization can be seen in Figures 2 and 3.

The reduction in coolant bulk temperatures (Fig. 2a) also significantly reduced the coolant pressure losses and the coolant convection heat transfer coefficients (Fig. 2b). This suggests that it might be possible to remove the heat transfer enhancements (mechanical wall turbulators) such as trip strips and impingement schemes from the coolant passages thus leading to a substantial reduction in turbine blade manufacturing costs.

The ultimate goal (reduction in the coolant mass flow rate) was achieved (Fig. 3a) by reducing the heat transfer coefficients and by making the passage walls thinner (Fig. 1b). It should be pointed out that the turbine inlet temperature changed very little when the maximum temperature equality constraint was enforced with this objective.

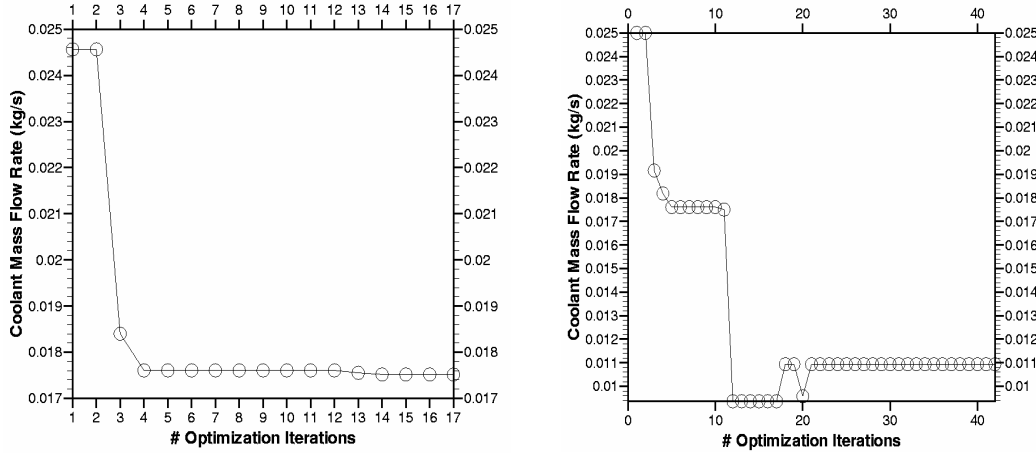


Figure 3: Evolution of coolant mass flow rate for the minimization of coolant ejection temperature using the maximum temperature equality constraint (left) and the maximum temperature inequality constraint (right).

But, when the maximum temperature inequality constraint was enforced, the coolant mass flow rate was reduced even more dramatically (Fig. 3b). However, the turbine inlet temperature decreased from 1600 K down to 1340 K which is unacceptable. The final optimized configuration had extremely thin walls and struts (Fig. 1b) which were nearly at the lower limits enforced by the bounds on their design variables. This configuration is clearly unacceptable because of the reasonable doubts if such a thin walled blade could sustain the mechanical stresses. It is interesting to note that the optimization with the maximum temperature inequality constraint ran for more cycles (40), but required fewer objective function evaluations (521). This was because of the fewer number of gradients needed for the inequality constraint functions. That is, the equality constraint was always active, but the inequality constraint was only active when the maximum temperature in the blade was equal to or greater than the specified maximum temperature,  $\overline{T}_{\max}$ .

*It can be concluded that even a seemingly minor change in the constrained multi-disciplinary (aero-thermal) optimization can have a profound influence on the acceptability of the optimized design. It can also be concluded that the hybrid constrained optimizer switching logic proved to be robust and efficient when solving a realistic problem.*

## 2. Thermal optimization of blades with a large number of cooling passages

The objective here is to minimize the total amount of heat transferred to the vane (integrated heat flux on the hot surface of the vane) while maintaining a maximum temperature,  $T_{\max}$ ,

which is lower than the maximum allowable temperature,  $T_{allow}$ . This objective indirectly minimizes the amount of coolant required to cool the vane. The minimization of this objective could result in the reduction of the number of cooling passages as well [6]. A numerical heat conduction analysis within the vane material is used to compute the objective and the temperature constraint. Instead of a fully 3-D conjugate heat transfer analysis [7] or a quasi 3-D conjugate heat transfer analysis [1] of each candidate vane configuration, heat convection boundary conditions were used to simulate the presence of coolant and hot gas. This approach includes a very approximate treatment of the fluid mechanics and excludes treatment of elasticity. However, it is sufficient for demonstrating the challenging nature of the design problem and the capabilities of the optimization algorithms used to solve the problem. The main difficulty in this design problem is due to the large number of design variables.

The objective function is computed by integrating heat flux across the vane outer surface,  $\Gamma$ . Mathematically, the objective function  $F$  is expressed as

$$F = \int_{\Gamma} k \frac{\partial T}{\partial n} dx dy dz \quad (1)$$

where  $T$  is the vane temperature,  $n$  is the direction normal to the surface  $\Gamma$ , and the constant  $k$  is the heat conduction coefficient for the vane material. There are two inequality constraints:

$$G_1 = \frac{T_{allow} - T_{max}}{T_{allow}} \quad (2)$$

$$G_2 = \sum_{i=1}^{nholes} C_i \quad (3)$$

where  $nholes$  is the number of passages and  $C_i$  is a positive number when the distance between passage  $i$  and another passage is less than a specified distance. Otherwise the value of  $C_i$  is zero. The first constraint is necessary so that the maximum temperature in the vane material is always below the maximum allowed temperature. The second constraint is needed to insure that the optimizer only searches for valid geometries. The constraints are satisfied if  $G_1 \leq 0.0$  and  $G_2 \leq 0.0$ .

The outer vane shape is considered to be fixed and to be provided by the user at the beginning of the design optimization. Presumably, this is the vane shape that has already been optimized for its aerodynamic performance. The design variables include the radius of each circular cross-section cooling passage,  $r_i$ , and position of each passage center,  $\langle x_i, y_i \rangle$ , in the vane cross-section. The passage centers are allowed to move normal to the outer contour within a specific region as shown in Figure 4.

The design variable  $x_i$  is a non-dimensional distance in the direction normal to the vane surface. The variable  $y_i$  is a non-dimensional distance in a surface-following coordinate direction that is taken along the outer surface of the vane. For 30 cooling passages, this parameterization leads to a total 90 design variables. A triangular surface mesh and a tetrahedral volume mesh were generated automatically for each candidate design. The mesh generator did an adequate job of placing enough points between the passages and the vane surface, even when the passages were very close to the surface. A typical mesh had around 80,000 nodes.

This design optimization problem was solved using both parallelized GA (PGA) [8] and IOSO [9]. The same initial design was given to both optimizers at the start of each run.

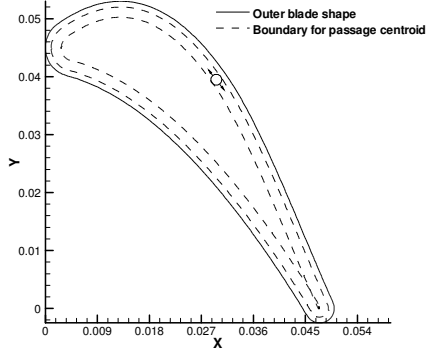


Figure 4: Region where coolant passage centers are allowed [6].

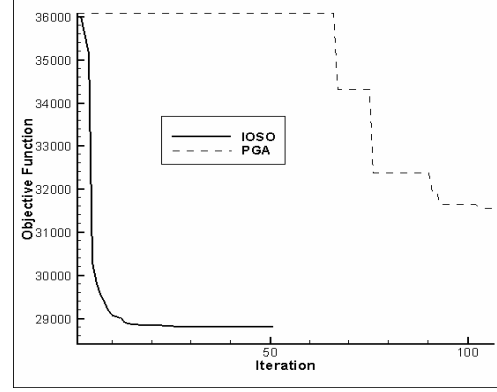


Figure 5: Objective function convergence history [6] with GPA and IOSO optimizers.

For both PGA and IOSO method, 40 configurations of cooling holes were analyzed simultaneously per iteration. Each finite element heat conduction analysis used 2 processors. The following PGA parameters were used: 5.0 percent mutation rate, 50.0 percent chance of uniform crossover, 7 bit binary encoding for  $y_i$  and 5 bit encoding for  $x_i$ ,  $r_i$ . A typical design optimization can be completed within a few hours using an inexpensive cluster of personal computers. For all cases the design variable bounds were set according to Table 1. Additional constants used for the example are shown in Table 2.

Table 1: Design variables

Variable	Lower bound	Upper bound
$r_i$	0.5 mm	0.8 mm
$x_i$	1.0 mm	1.525 mm
$y_i$	$\frac{y_{i-1} + y_i}{2}$	$\frac{y_i + y_{i+1}}{2}$

Table 2: Constants used for design examples

Max. allowable temperature, $T_{allow}$	900.0 °C
Vane heat conduction coefficient, $k$	9.0 W/m-°C
Vane span, $L$	5.0 cm
Vane axial chord length	5.0 cm
Minimum allowable distance between passages	0.1 mm

The convergence history (Fig. 5) shows that for this example the IOSO method outperforms the PGA method. Both IOSO and PGA methods reduced the total heat flux from the initial design as shown in Table 3. The IOSO optimization method was found to produce better results with fewer iterations than the PGA method. The IOSO method is also more robust and easier to use since it requires fewer tuning parameters than the PGA method.

Table 3: Optimization results.

Result	Initial guess	PGA best design	IOSO best design
$n_{holes}$	30	30	30
$T_{max}$	892.6 °C	899.1 °C	902.3 °C
$F$	36099.8 W	31563.0 W	28808.2 W

Specifically, one can see (Fig. 6) that the topology of the passages is slightly different between the two best designs. The result of the PGA is clearly at a local optimum since some passages are clustered too closely together near the leading and trailing edge creating overcooled areas. The passage size and position for the IOSO result is more uniform than the PGA result. More iterations and more fine-tuning of control parameters, including increasing the selection pressure, could improve the PGA result.

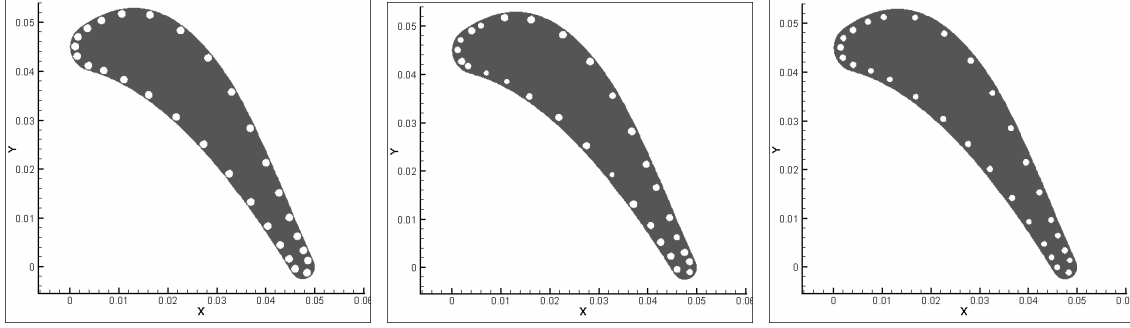


Figure 6: Cooling passages for initial design (left), PGA best design (middle), and IOSO best design (right) for a case with 30 cooling passages [6].

The outer blade surface temperature on the optimized design is much closer to  $T_{allow}$  than in the initial design. The best possible design could be achieved if the entire outer surface temperature would be equal to  $T_{allow}$ . In that case, the smallest possible integrated heat flux would be 19830.0 W. However, a perfect design is not achievable due to the limitations of the geometric parameterization. The next step towards a complete automatic design system should be to add 3-D fluid mechanics analysis codes and 3-D thermoelasticity analysis thus providing a fully 3-D conjugate analysis environment. However, this would then increase computing time by an order of magnitude. But, with the recent availability of a low cost parallel supercomputing based on commodity component, a complete multi-disciplinary design system may be proven to be computationally and financially feasible in the very near future.

### 3. Thermo-elasticity optimization of 3-D serpentine cooling passages in turbine blades [12]

An automatic design algorithm for parametric shape optimization of three-dimensional cooling passages inside axial gas turbine blades has been developed. The outer blade geometry was created by generating a series of two-dimensional turbine airfoils [10] and stacking the sections along the  $z$ -axis. Smooth serpentine passage configurations were considered. The geometry of the blade and the internal serpentine cooling passages were parameterized using surface patch analytic formulation [11], which provides very high degree of flexibility, second order smoothness, a minimum number of parameters, and guarantees minimum wall thickness. The design variable set defines the geometry of the turbine blade coolant passage including blade wall thickness distribution and blade internal strut configurations. All together a total of 42 continuous design variables were used to uniquely describe a design [12].

A parallelized 3-D thermoelasticity finite element method (FEM) computer code from the ADVENTURE project at the University of Tokyo [13] was used to perform automatic thermal and stress analysis of different blade configurations. The root section of the geometry was set to zero displacement while the blade and inner shroud were left free to deform. In this simplified problem the aerodynamic loads are not included. As for thermal boundary conditions, the outer surface of the blade and top surface of inner shroud were set to convection boundary conditions which require the specification of the convection coefficient,  $h_B$ , and the hot gas bulk temperature,  $T_B$ . Convection boundary conditions were also applied to the coolant passage surface inside the blade using  $h_C$  and  $T_C$ . All other surfaces were assumed thermally insulated. Both centrifugal and thermal body forces were applied automatically to each design mesh. The objective of the optimization was to make stresses throughout the blade as uniform as possible. Constraints were that the maximum stress and temperature at any point in the blade were less than the maximum allowable values. A robust semi-stochastic

constrained optimization algorithm (IOSO) and a parallel genetic algorithm (PGA) were used to solve this problem while running on an inexpensive distributed memory parallel computer.

The objective of the design optimization was to minimize the variation in stress distribution within the blade material. The normalized objective function was computed using the maximum principal stress at each node within the blade.

$$F = \sum_{i=1}^n \frac{\sigma_i^2}{n \sigma_{yield}} \quad (4)$$

where  $\sigma_i$  is the maximum principal stress at node  $i$ ,  $n$  is the number of computational grid points within the blade, and  $\sigma_{yield}$  is the yield stress of the blade material. Only nodes within the blade itself are considered for the objective and constraint functions. By minimizing this objective function, a smoothing effect on the principal stress field is achieved. This objective also drives the stresses to lower values, which is also desirable for the durability of the blade.

In addition to minimizing the objective function, the optimizer must find a design that simultaneously satisfies the design constraints. For the design of a turbine rotor blade, the maximum temperature should be less than an allowable temperature,  $T_{allow}$ . Similarly, the maximum principal stress should be less than the yield stress,  $\sigma_{yield}$ . These two inequality constraints are expressed mathematically as

$$G_1 = \sum_{i=1}^n \frac{1}{n} \left[ 100 .0 \frac{(\bar{T}_i - T_{allow})}{T_{allow}} \right]^2 \quad (5)$$

$$G_2 = \sum_{i=1}^n \frac{1}{n} \left[ 100 .0 \frac{(\bar{\sigma}_i - \sigma_{yield})}{\sigma_{yield}} \right]^2 \quad (6)$$

where the constraints are satisfied if  $G_1 \leq 0.0$  and  $G_2 \leq 0.0$ , while

$$\bar{T}_i = \begin{cases} T_i & \text{if } T_i > T_{allow} \\ T_{allow} & \text{if } T_i \leq T_{allow} \end{cases} \quad (7)$$

$$\bar{\sigma}_i = \begin{cases} \sigma_i & \text{if } \sigma_i > \sigma_{yield} \\ \sigma_{yield} & \text{if } \sigma_i \leq \sigma_{yield} \end{cases} \quad (8)$$

The above constraints on maximum temperature and maximum stress could have been written more simply as

$$G_1 = T_{max} - T_{allow} \quad (9)$$

$$G_2 = \sigma_{max} - \sigma_{yield} \quad (10)$$

where  $T_{max}$  and  $\sigma_{max}$  are the maximum nodal temperature and principal stress, respectively. However, constraints (5)-(6) have the effect of penalizing designs with many nodes with

infeasible temperature or stress, where as constraints (9)-(10) only consider the worst values at a single node. We found that the constraints (9)-(10) worked well only when an initial feasible design was given at the start of the optimization. In cases where no initial feasible design was known, the constraints (5)-(6) produced superior results in fewer iterations for both PGA and IOSO algorithms.

If a large number of processors are available, the optimizer can use all of them by running several simultaneous parallel analyses to evaluate several candidate design configurations. For this research an optimization communication module was developed using the MPI library [14] that utilizes this multilevel hierarchy of parallelism. This module can be used with any parallel optimization method including PGA and IOSO algorithms.

The optimization run was performed on a commodity component based on an older PC cluster with 54 Pentium II 400 MHz processors. Both PGA and IOSO optimization methods were tested with this problem. A total of 12 analyses were performed per iteration for IOSO method. For PGA, 36 designs were evaluated per generation. For both cases each parallel thermoelastic FEM analysis used 4 processors. A typical analysis mesh contained over 150,000 degrees of freedom and required 4 minutes to complete a full thermoelasticity analysis. A converged result was found by the IOSO optimizer in 70 iterations after consuming approximately 12 hours of total computer time. For PGA, the total computer time was more than 30 hours. The PGA run was terminated before a converged result was found.

The convergence history for the objective function for both PGA and IOSO is shown in Figure 7. For all designs the stress constraint was satisfied. However, the initial design violated the temperature constraint so the optimizer had to first determine a feasible design. The convergence history for the temperature constraint function is shown in Figure 8. This figure shows that a feasible region was found at iteration 12 for IOSO and iteration 68 for PGA. For the IOSO method, after iteration 12 the best design becomes the feasible design, which is why a spike in Figure 7 occurs at iteration 12. Prior to that, only infeasible designs were found and the optimizer clearly tried to improve the objective function while searching for the feasible region. These convergence results clearly show the computational efficiency of the IOSO approach over the PGA method for this design problem.

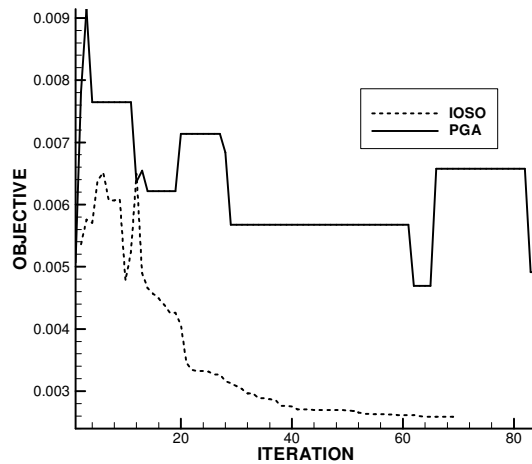


Figure 7: Objective function convergence history [12].

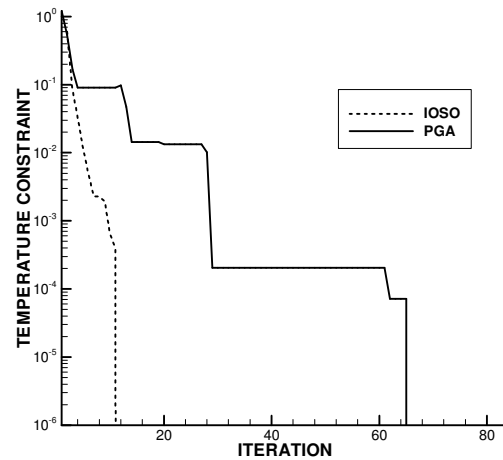


Figure 8: Temperature constraint function [12].

The initial and the IOSO optimized passages configurations are shown in Figures 9. The wall near the tip corners has become much thinner in an effort to keep the temperature in those regions below the maximum allowable value.



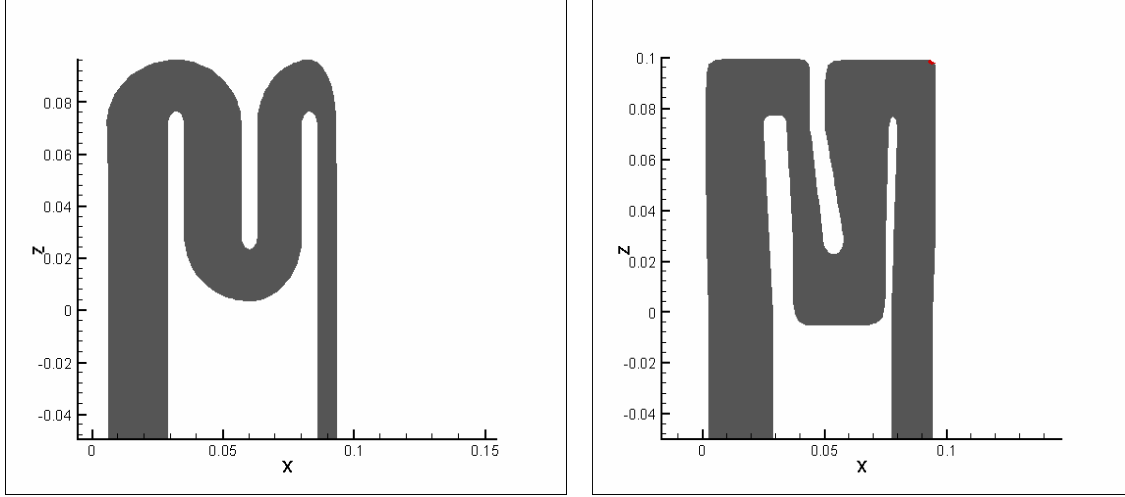


Figure 9: Initial shape (left) and IOSO optimized shape (right) of the 3-D cooling passage.

Table 4: Comparison of initial and optimized cooling passage design

Quantity	Initial	Optimized
Maximum Temperature, $T_{max}$	1333.8 °C	894.6 °C
Volume	$9.64 \times 10^{-4} \text{ m}^3$	$8.46 \times 10^{-4} \text{ m}^3$
Maximum Principal Stress, $\sigma_{max}$	668.9 MPa	425.1 MPa
Coolant bulk temperature, $T_C$	600.0 °C	158.0 °C
Objective function value, $F$	$6.80 \times 10^{-3} \text{ Pa}$	$2.59 \times 10^{-3} \text{ Pa}$

The volume of the optimized blade is slightly smaller than the initial design (Table 4), most likely due to the thinning of the walls in the tip region of the blade. The optimized design's maximum principal stress was reduced by 36 percent and its objective function reduced by 62 percent. The optimizer reduced the coolant temperature design variable,  $T_C$ , from 600.0 °C to 158.0 °C. The reduction in coolant temperature was necessary for the satisfaction of the maximum temperature constraint. Although the temperature difference between the coolant and outer hot gas increased, the thermal stresses actually decreased. The most significant thermal stresses appear to be the result of temperature distribution along the span and chord direction. Therefore the optimizer determined the wall thickness distribution such that the variation of temperature in the chord and span direction was reduced.

Principal stresses on the surface of the blade with the initial shape of the coolant passage is shown in Figure 10, while the IOSO optimized coolant passage offers lower and more uniform stress field (Figure 10). Stress in the root of the blade is high due to the centrifugal loading and temperature gradients.

Temperature distributions for the initial design and the IOSO optimized design are shown in Figures 11 and 12. The temperature patterns on the surface of the blade follow the shapes of the passage inside the blade. This shows that the passage shape will have a strong impact on the temperature distribution and hence the thermally induced stresses. The temperature distribution on the surface of the IOSO optimized blade is considerably lower and smoother compared with that of the initial design.

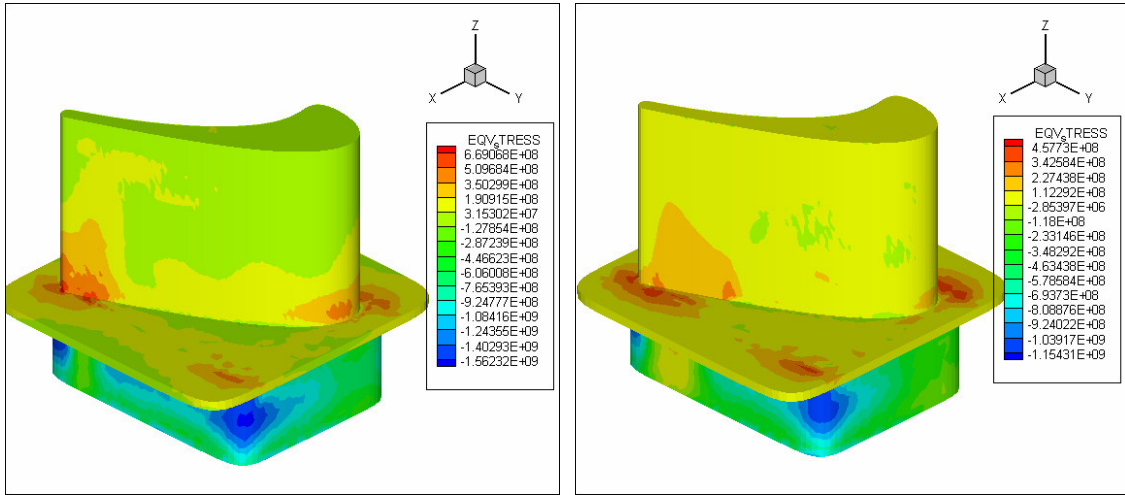


Figure 10: Principal stress contours for initial (left) and IOSO optimized design (right).

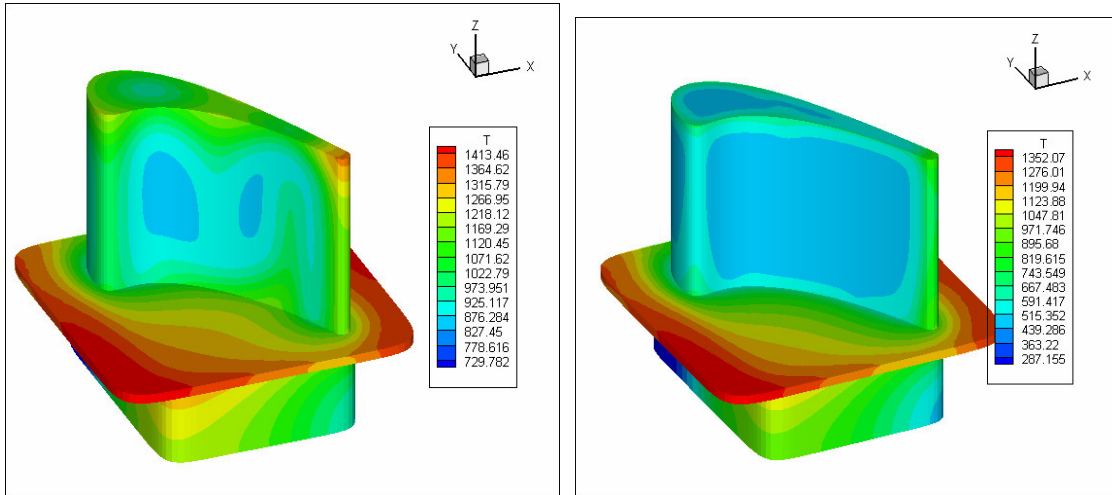


Figure 11: Surface temperature field on pressure side for the initial cooling passage shape (left) and for IOSO optimized design of 3-D cooling passage (right).

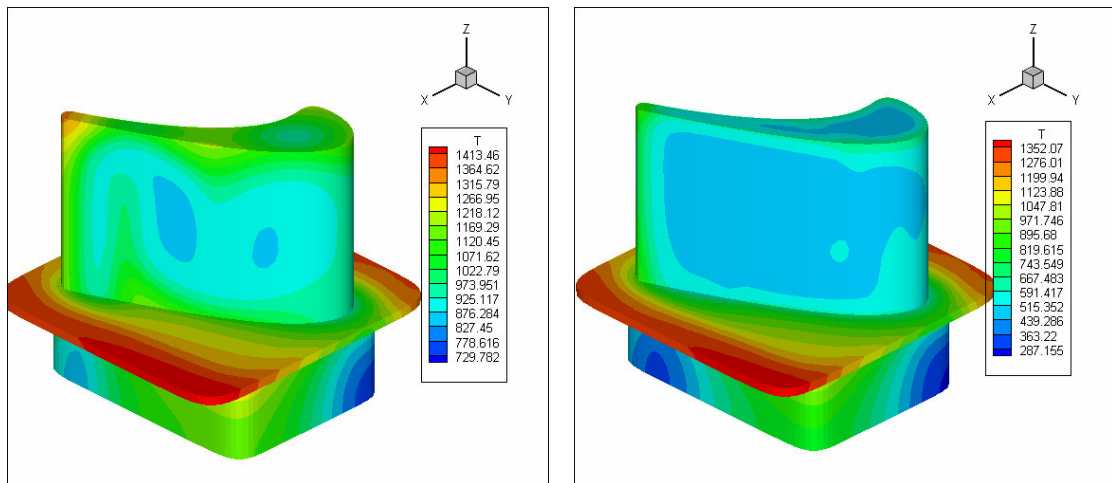


Figure 12: Temperature contours on suction side for IOSO optimized design.

## 4. Aero-thermo-structural optimization of internal coolant networks in turbine blades

This section presents the theoretical methodology, conceptual demonstration, and validation of a fully automated computer program (Fig. 13) for the inverse design and optimization of internal convectively cooled 3-D axial gas turbine blades [1,4]. A parametric computer model of the 3-D internal cooling network was developed including the automatic generation of computational grids. A boundary element computer program was written to solve the steady-state non-linear heat conduction equation inside the internally cooled and thermal barrier-coated turbine blade. A finite element algorithm was written to model an arbitrary network of internal coolant passages for the calculation of the internal pressure losses, flow rates, the effects of centrifugal pumping, heating of the coolant fluid, and heat transfer coefficients from the thermal model of the solid to the coolant fluid.

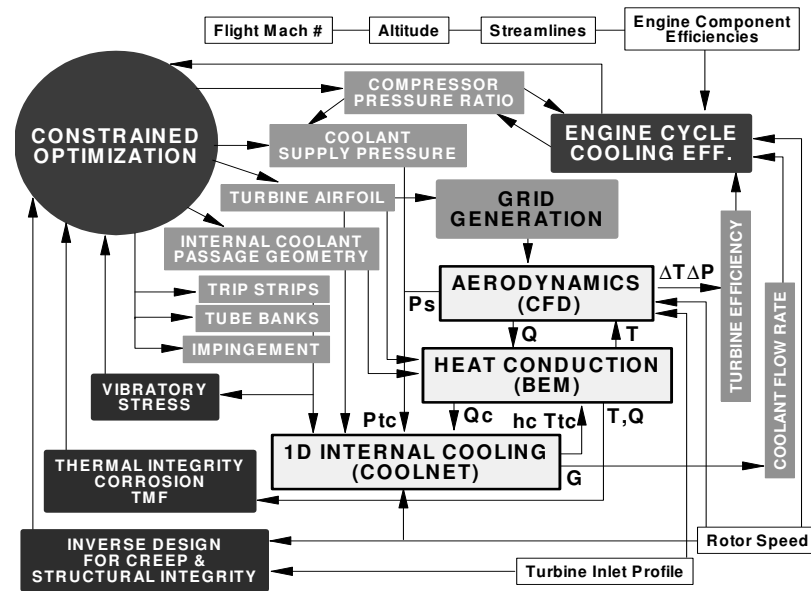


Figure 13: Flow chart for the multi-disciplinary design and optimization of internally cooled turbine airfoils.

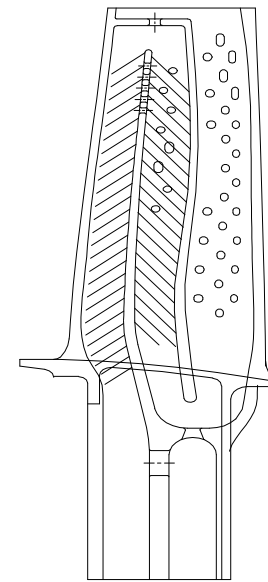


Figure 14: Cross-section schematic of the P&W F100 second rotor blade.

The heat conduction and internal flow analyses were strongly and iteratively coupled to account for the heat balance between the blade and the coolant fluid. Our hybrid optimization system (older version) was used to modify the internal cooling configuration and internal heat transfer enhancements (boundary layer trip strips and pedestals) in order to achieve the objectives of increased cooling effectiveness and greater durability against oxidation, corrosion and creep. The computer-automated design and optimization system was demonstrated on the second row of high-pressure turbine of the Pratt & Whitney F100 engine (Fig. 14). The internal cooling optimization on the product definition of this blade yielded a 5 percent increase in average cooling effectiveness with only a marginal increase in coolant flow rate, in addition to having the same corrosion life and a doubling of the creep life.

### 4.1. Design of turbine blades for structural integrity and creep life

In cooled turbine blade design, the forward design process begins with the generation of an internal cooling scheme and then the stresses or temperatures are calculated later using some

analysis tool. Inverse design works in the opposite direction. That is, having knowledge of the temperature or stress field; it is possible to determine an unknown geometry that is compatible with this stress and temperature data. Inverse design is possible only if some additional information, albeit approximate and *a priori*, is available in addition to what would be boundary conditions of a well-posed (forward) problem. For example, it is well understood that the stress at the blade root may not exceed the yield stress,  $\sigma_y$ . Blades are also designed to have a certain life span that is severely limited by temperature-dependent creep. The designer also needs to know something about the radial variation of the blade temperature so that the internal cooling scheme can be designed to maintain a certain average creep life requirement. That is, the average creep life of the blade is specified first. Then, after computing the radial variation of the centrifugal stress limit from this requirement, the thickness of the coolant passage wall is determined so as not to exceed the centrifugal stress limit.

Given the non-uniform combustor exit flow profile, the hottest gases in the turbine tend to migrate to the mid-span radius, while the centrifugal stresses in the blade are the highest at the root of the blade and decrease radially. The combined 3-D temperature and stress environment provides that the worst creep is experienced at some critical span location. Thus, a radial gas temperature profile,  $T_G(r)$ , from a CFD calculation was used to approximate a radial variation of the blade's metal temperature,  $T_m(r)$ . This required some approximate knowledge of the average heat transfer coefficients pre-calculated or assumed on the blade's external surface,  $h_G$ , and on the internal coolant passage surfaces,  $h_C$ . A nominal blade wall thickness,  $t_m$ , a nominal thermal barrier coating thickness,  $t_o$ , and a bulk coolant temperature,  $T_C$ , were also needed. The spanwise variation of wall temperature can be computed from the following approximate expression.

$$T_m(r) = \frac{h_G T_G \left(1 + \frac{h_C t_m}{k_m}\right) + h_C T_C \left(1 + \frac{h_G t_o}{k_o}\right)}{h_G \left(1 + \frac{h_C t_m}{k_m}\right) + h_C \left(1 + \frac{h_G t_o}{k_o}\right)} \quad (11)$$

Here,  $k_m$  and  $k_o$  are the coefficients of thermal conductivity of the metal and thermal coating, respectively. The internal heat transfer coefficients,  $h_C$ , and bulk coolant temperatures,  $T_C$ , did not have radial or passage-to-passage variations either, so only average values were used.

With this approximate blade surface temperature variation,  $T_m(r)$ , and a given average creep life of the blade,  $\dot{\epsilon}_C$ , the radial variation of the allowable centrifugal stress in the blade metal was estimated using the Larson-Miller relation where the mean creep life was quantified by a function of stress, temperature and time [15]. The following equation was experimentally derived to relate creep rate to temperature and stress [16].

$$\log(\dot{\epsilon}_C) = C_0 + \frac{C_1}{T} + C_2 \log \left[ \sinh \left( \frac{C_S \sigma}{E} \right) \right] \quad (12)$$

In this equation,  $\sigma$  is the stress and  $C_0$ ,  $C_1$ ,  $C_2$  and  $C_S$  are constants. This equation was solved for  $\sigma$  (now called  $\sigma_{r,max}$ , given  $T_m(r)$  for  $T$ ) from the critical span (radial location of the blade that has the highest metal temperature) out to the blade tip. For the rest of the blade, the maximum allowable stress,  $\sigma_{r,max}$ , was linearly increased from the stress at the critical span to the tensile yield stress,  $\sigma_Y$ , at the root.

An iterative root-finding inverse design procedure was used to determine the radial variation of the coolant passage wall and internal rib thicknesses. In this iterative procedure,

the two-dimensional turbine blade sections were generated from the tip to the root, while the nominal wall thicknesses were increased when the calculated centrifugal stress exceeded the specified allowable stress from equation (12). The resulting parametric blade representation was implicitly able to maintain the centrifugal loads as well as meet the creep life constraint (assuming some margin of errors caused by three-dimensionality, hot gas migration, thermal mixing, uncertainty in geometry and operating conditions, etc). In the design of this turbine blade, a +/- 5 to 10 percent margin of error in coolant flow rate was accounted for with a 5 percent margin of error in metal temperature ( $T_m$ ).

Assuming that the external aero-thermodynamics is fixed and there is no film cooling, the optimization objective function took the form of a thermal-only optimization function. For internal convective cooling schemes, an optimization objective can be mathematically formulated as the maximization of the cooling effectiveness or convective efficiency.

$$F(\vec{V}) = \phi = \int_{\Gamma_E} \frac{T_G - T}{T_G - T_{t,c}} d\Gamma \quad (13)$$

In this equation,  $T_{t,c}$  is the coolant total temperature at the inlet to the coolant passages,  $T$  is the metal temperature, and  $\Gamma_E$  indicates the external surface of the turbine blade. Maximization of this objective function drives the temperature of the turbine blade or vane towards the coolant temperature, thus improving its durability. But, this function has no penalizing effect to compensate for the fact that increased coolant flow rates may worsen the engine cycle efficiency, and that increased supply pressure causes greater leakage losses. On the other hand, if the coolant supply temperature,  $T_{t,c}$ , is a degree of freedom, the process of minimizing the cooling effectiveness may drive the coolant temperature higher because enhancements to the internal heat transfer coefficients are correlated with higher pressure losses. Therefore, the bleed air must be taken from higher compressor stages where the air temperatures are higher because of compression and because these stages are in closer proximity to the burner. The use of the convective efficiency objective function has an element of risk and so should be penalized by the supply coolant pressure and/or coolant flow rate. For example, one such penalized objective function that could be minimized for a coolant effectiveness optimization is

$$F(\vec{V}) = \frac{G_c}{\phi P_{t,c}} \quad (14)$$

In this equation,  $G_c$  is the internal coolant flow rate,  $\phi$  is the convective efficiency, and  $P_{t,c}$  is the total pressure at the inlet to the coolant passages.

The material integrity and blade durability against oxidation and corrosion were maintained with a constraint function by ensuring that the maximum temperature in the blade material did not exceed its thermal or corrosion life limit,  $\overline{T_{max}}$ . Thus, the optimization constraint function for thermal integrity was formulated as follows.

$$G(\vec{V}) = \frac{T_{max}}{\overline{T_{max}}} - 1 \leq 0 \quad (15)$$

Internally cooled turbine blade configurations were said to be feasible whenever this condition was satisfied, in addition to the other constraints such as aerodynamic loads, structural integrity, and when the coolant air bleed pressure was high enough to drive the internal coolant flow.

## 4.2. Internal coolant network aero-thermal analysis

The internally cooled turbine blade problem involves a complex internal coolant flow network with many branches. Methods for calculating flow rate and pressure losses in such a system are similar to methods for analyzing electrical networks, but it is highly nonlinear and a large number of parameters have a significant effect on the energy conservation and flow losses. With the addition of complex heat exchangers, banks of pedestals, rows of skewed internal ribs or trip strips, 180° bends, internal impingements and other heat transfer enhancements, the quasi one-dimensional prediction of internal compressible flow losses and coolant fluid heating must be correlated with a great deal of empirical data over a broad range of operating conditions, configurations, and characteristics. A quasi one-dimensional compressible thermo-fluid flow network program (COOLNET) [4] was written in the Fortran programming language to predict coolant flow rate,  $G_c$ , total coolant pressures,  $p_t$ , bulk coolant total temperatures,  $T_{t,c}$ , and internal heat transfer coefficient distributions,  $h_c$ , inside internally cooled turbine blades and vanes. It was written as a generalized program for thermo-fluid elements and adapted into the computer-automated design system for optimization. The coolant passages were allowed to be an arbitrary network of one-dimensional fluid elements or tubes. The lengths, cross-sectional areas, perimeters, wall roughness, heat transfer enhancements, etc. were specified uniquely for each fluid element. This locally one-dimensional geometric information was mapped automatically from the three-dimensional parametric model to the input of the COOLNET algorithm.

The FEM solved the thermo-fluid network problem for specified inlet relative total pressures, inlet relative total temperatures, and exit static pressures. The equations were solved by a Picard iteration strategy due to the nonlinearity of the pressure loss functions. The stability and convergence of the solution technique depended on the accuracy of the initial guess for the local mass flow rates. Under-relaxation was used when updating the flow rates,  $G_m$ , in each fluid element. The initial guess to the internal coolant flow rates was set up using local area-weighted flow splitting at each nodal junction connecting three or more coolant fluid elements.

The relative total pressure drop,  $\Delta P_t$ , across each element that rotates with angular speed  $\Omega$ , is governed by the momentum conservation equation. Pressure changes due to friction,  $\Delta P_f$ , acceleration of the flow by heating,  $\Delta P_a$ , and centrifugal pumping,  $\Delta P_c$ , are summed up as the total pressure change between nodes 1 and 2 [1,4].

$$A_2 P_{t,2} - A_1 P_{t,1} = S \Delta P_f + A (\Delta P_a + \Delta P_c) \quad (16)$$

Here,  $A$  is the cross-sectional area and  $S = \text{Per} \cdot \text{Len}$  is the surface area (perimeter times length) of the element. The pressure loss due to friction,  $\Delta P_f$ , is proportional to the dynamic pressure. The pressure change due to centrifugal pumping,  $\Delta P_c$ , was derived from the momentum equation in cylindrical coordinates. The flow accelerates when heat is added to the fluid, so the pressure change due to heating is included with the addition of the term,  $\Delta P_a$ . Hence, the three kinds of total pressure change are given as follows:

$$\Delta P_f = -C_f \frac{1}{2} \rho v^2 \quad (17)$$

$$\Delta P_a = \frac{\gamma}{2} M^2 \frac{(T_{r2} - T_{r1})}{T_r} P_t \quad (18)$$

$$\Delta P_c = \rho R \Omega^2 (R_2 - R_1) \quad (19)$$

Here,  $C_f$  is the friction coefficient,  $\rho$  is the coolant density,  $v$  is the local coolant speed,  $M$  is the local coolant Mach number,  $T_{rt}$  is the relative total temperature of the coolant,  $\gamma$  is the ratio of specific heats,  $R$  is the radius from the engine centerline, and  $P_t$  is the relative total pressure of the coolant. When the element was an exit path, the total pressure was related to the static (dump) pressure. In order to model these elements, the friction coefficient was set to unity,  $C_f = 1.0$ . A discharge coefficient,  $C_D$ , was also needed to determine the actual film cooling flow rates.  $C_D$  was defined as the ratio of the actual mass flow rate,  $G$ , to the ideal mass flow rate. The ideal mass flow rate was calculated by assuming an isentropic one-dimensional expansion from the total pressure,  $P_t$ , to the static pressure,  $P_s$ .

$$C_D = \frac{G}{P_t \left( \frac{P_s}{P_t} \right)^{\frac{\gamma+1}{2\gamma}} A \sqrt{\frac{2\gamma}{(\gamma-1)RT_t} \left[ \left( \frac{P_t}{P_s} \right)^{\frac{\gamma-1}{\gamma}} - 1 \right]}} \quad (20)$$

Equation 18 was used to calculate the mass flow rates during the iterative solution procedure. Discharge coefficients were dependent on local coolant passage geometry as well as internal and external flow conditions [1,4]. The mass flow through the element,  $G = \rho A v$ , is an unknown in this system. Continuity gives equilibrium conditions at the nodes of the fluid network. Here,  $G_m$  is positive entering the node and negative leaving the node. The summation is over each  $m$ -th element attached to the node.

$$\sum_m G_m = 0 \quad (21)$$

The  $N_{FE}$  elemental pressure balance equations were cast into a local FEM matrix form.

$$\left[ \begin{array}{ccc} \frac{2A_1}{C_f v} & -\frac{2A_2}{C_f v} & -1 \end{array} \right] \left\{ \begin{array}{c} P_{t,1} \\ P_{t,2} \\ G_{12} \end{array} \right\} = -\frac{2A}{C_f v} [\Delta P_a \quad \Delta P_c] \quad (22)$$

Here,  $G_{12} = -G_{21}$ . The  $N_{FE}$  local FEM pressure balance equations were combined with the  $N_{FN}$  nodal equilibrium equations to form a global FEM system. Pressure boundary conditions were applied at the inlet and exit (source and sink) nodes of the network. It was standard practice to apply total pressures,  $P_{t,i}$ , at all inlet nodes and static pressures,  $P_{s,j}$ , at all exit nodes, where  $i = 1, \dots, N_{IN}$  and  $j = 1, \dots, N_{EX}$ . The fluid network was allowed to have an arbitrary number of inlet nodes,  $N_{IN}$ , and exit nodes,  $N_{EX}$ . The equilibrium equations were written only at the internal nodes since they are not applicable at inlet and exit nodes. If the network had  $N_{IN}$  inlets and  $N_{EX}$  exits, the global finite element system had an equal number,  $(N_{FE} + N_{FN} - N_{IN} - N_{EX})$ , of equations and unknowns that were solved for the unknown total pressures at each internal node and local coolant flow rates in all elements.

The 3-D enthalpy conservation equation was solved to calculate the bulk coolant total temperatures,  $T_{t,c}$ , of the convecting and rotating coolant fluid. Convective heat transfer through the walls of the coolant flow passage,  $Q_c$ , accounted for heat addition. The energy equation for the cooling air was expressed in local finite element matrix form in terms of total rothalpy,  $H_r$ , [17].

$$\begin{bmatrix} G & -G \\ -G & G \end{bmatrix} \begin{Bmatrix} H_{r,1} \\ H_{r,2} \end{Bmatrix} = \begin{Bmatrix} -Q_c S \\ Q_c S \end{Bmatrix} \quad (23)$$

Here,  $S$  is the surface area exposed to the coolant fluid. The total rothalpy [17] at each node is defined by

$$H_r = C_p T_c + \frac{1}{2} v^2 - \frac{1}{2} r \Omega^2 \quad (24)$$

where  $C_p$  is the specific heat,  $T_c$  is the bulk coolant static temperature,  $r$  is radius from the engine centerline, and  $\Omega$  is the rotor speed. The heat flux,  $Q_c$ , was obtained by a three-dimensional BEM analysis of the heat conduction in the turbine blade. The system of equations (13) was generated for each fluid element and assembled into a global system using the FEM. The solution of this system required that the bulk total temperature of the coolant,  $T_{t,c}$ , be specified at all inlet paths.

The global pressure and rothalpy systems resulted in coefficient matrices that needed to be inverted at every iteration of the COOLNET algorithm. The pressure system was slightly ill conditioned when large complex internal networks were solved, so the Singular Value Decomposition [18] was used to invert that matrix. The result of these matrix inversions were values of the total pressure at every internal node, the mass flow rate through every element, and the rothalpy at every internal and exit node.

In an effort to enhance heat transfer, modern cooling designs utilize turbulators such as trip strips or transverse ribs in order to increase the internal heat transfer coefficients. They induce early transition to turbulence and greatly increase the channel friction and pressure losses, while moderately increasing the convective heat transfer. A large number of heat transfer and pressure loss correlations appear in the open literature and in textbooks. Several of those that pertain to internal cooling of turbine blades have been adapted into this research and used to predict pressure losses and heat transfer coefficients by COOLNET.

#### 4.3. Validation of the internal coolant network flow solver and conjugate analysis

The thermo-fluid network flow solver was verified against data from a bench test of a sterolithography model. The second rotor blade of the Pratt & Whitney F100 engine was used for this purpose. This blade utilizes a three-pass serpentine design with two feed passages and ejection of the internal cooling air at the tip. The internal configuration is illustrated in Figure 14, and the internal coolant network of fluid elements used by COOLNET is shown in Figure 15. The first up-pass and the down-pass were enhanced with boundary layer trip strips (TRP). The second up-pass had a bank of pedestals (PED) that have been oriented in a certain pattern to avoid vibratory stresses. The pedestals were either circular or oblong circular shape. The coolant air is ejected at the tip of the blade and into the tip pocket. Several bleed holes (BLD) across the leading edge rib reduce the pressure losses around the first tip turn. Pressure taps were used to measure internal pressures and a Pratt & Whitney proprietary flow model was calibrated to this data.

COOLNET solved for the relative total pressures and total temperatures in about forty iterations. At the starting point of the iterative solution process, the inlet flow rates were assumed to have a Mach number of 0.1 in the feed paths (number 101 and 102) and area-based flow splitting was used to establish the remaining elemental flow rates. Figure 6 illustrates the convergence rate for the maximum wall temperature, coolant total temperature and coolant flow rate versus conjugate iteration number. Each conjugate iteration number is defined as one external CFD analysis with SWIFT using applied airfoil wall temperature variation, one



thermal-fluid analysis of the internal coolant network with variable heat flux applied, and one BEM heat conduction analysis with applied external and internal heat transfer coefficients and internal bulk coolant temperatures. The convergence is rapid and stable because the non-linearity is weak (Fig. 16). After six iterations, the maximum change in wall temperature is approximately 0.25 K, the maximum change in cooling air temperature is approximately 0.12 K, and the change in total cooling airflow is approximately 0.002 percent.

**F100-2B**

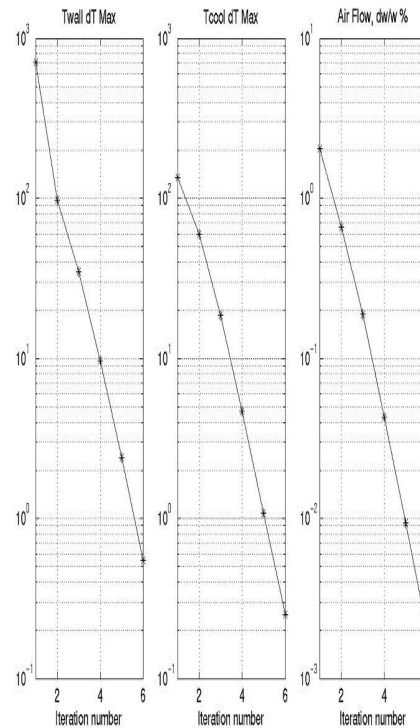
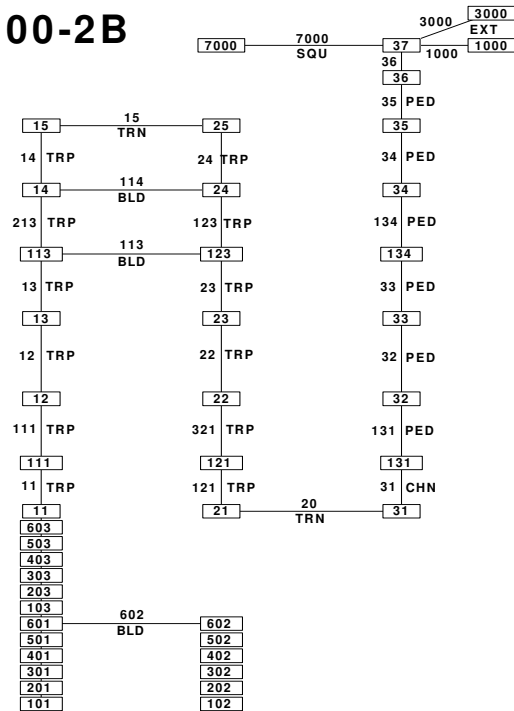


Figure 15: COOLNET internal flow network model for the P&W F100 second rotor blade of a high pressure turbine	Figure 16: Convergence rates for the maximum wall temperature, coolant total temperature and coolant flow rate versus conjugate iterations.
---	---

Each fully-coupled 3-D prediction of the temperature field using the aero-thermal-fluid system required about 25 minutes of CPU time on a Sun Ultra-60 workstation (equivalent to less than 5 minutes on a 1.7GHz Intel Xeon).

The results of the COOLNET computation are shown against the data from a Pratt & Whitney internal flow design code calibrated to the experimental pressure tap data in Figures 17 and 18. These figures show only data in the coolant flow passages above the platform.

Thus, elements 11 to 14 are shown with boxes, elements 24 to 141 are shown with circles, and elements 31 to 36 are shown with diamonds. Because the actual values of the data are company sensitive, the axis labels have been removed. Notice though that the trends and magnitudes are within acceptable limits.

The main problem with the COOLNET algorithm was that it tended to predict a slightly higher flow rate (about 9-10 percent). This resulted in higher-pressure losses and lesser coolant fluid heating in all passages. The cause of this discrepancy is probably due to the fact that the discharge coefficients of the bleed holes in the Pratt & Whitney model were  $C_D = 0.9$ . In COOLNET, the bleed paths (BLD) were modeled as smooth channels and nothing special was done at the inlet paths (number 101 and 102). Both COOLNET and the Pratt & Whitney internal flow design code predicted that the exit flow path, SQU that dumps the air into the tip

pocket had reversed, and that path 7000 was actually feeding the system. This effect appears in Figure 8 in the upper right hand corner.

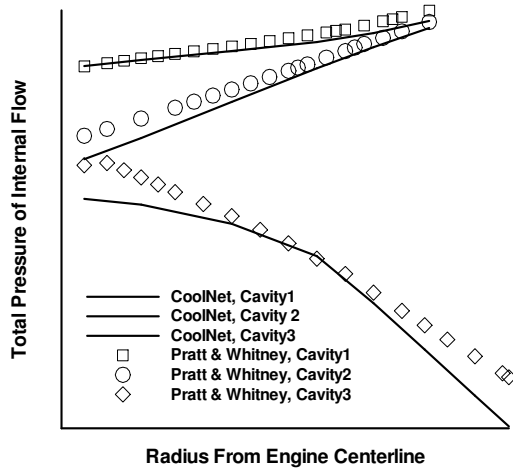


Figure 17: Comparison of spanwise distribution of total pressures of internal coolant flow predicted by COOLNET versus Pratt & Whitney internal flow design code calibrated to experimental pressure tap data inside F100 second blade.

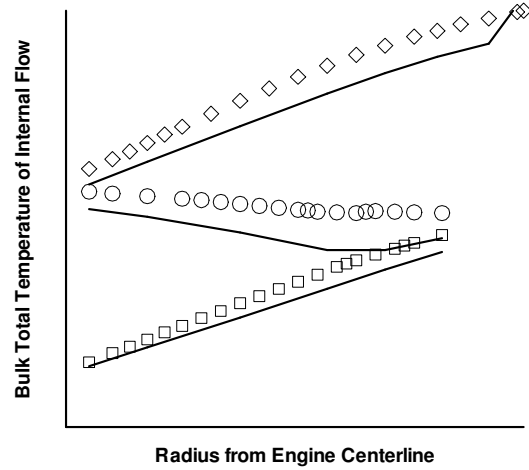


Figure 18: Comparison of spanwise distribution of total temperatures of internal coolant flow predicted by COOLNET versus Pratt & Whitney internal flow design code calibrated to experimental pressure tap data inside F100 second blade.

#### 4.4. Cooling effectiveness optimization

The computer-automated design and optimization system was demonstrated on the second high-pressure turbine blade of the Pratt & Whitney F100 engine. The fully 3-D geometry of the coolant passages and internal heat transfer enhancements were optimized for maximum cooling effectiveness at a fixed coolant flow rate by minimizing equation (13). The external aerodynamics and coolant supply pressure were held fixed during the optimization process, while parameters such as rib turbulator height, turbulator pitch, pedestal diameter and internal rib positions were allowed to vary.

The optimization started from a blade that was very similar to the actual product definition of the P&W F100 second turbine blade (Fig. 14). The inverse shape design procedure was used to maintain creep life and structural integrity. The rib thicknesses and coolant wall thickness distribution were increased from the tip to the root to maintain the centrifugal load and creep life. With the generation of each new parametric design, the radial variations of wall rib thickness were adjusted to reproduce the same radial centrifugal stress variation in the blade.

The entire 3-D blade was redesigned with 24 optimization design variables at five spanwise sections (Table 5). The two internal ribs of the actual design were initially vertical. During the optimization, five 2-D design sections controlled the rib positions. The die pull angles of both ribs were also part of the design variable set, but fixed radially in order to account for cast-ability. The internal coolant walls were enhanced with two sets of ribbed turbulators (trip strips) for each leading and mid-body coolant passages. The strips of boundary layer turbulators were placed on the suction and pressure sides along the entire radial span of the two passages up until the first tip turn. The heights, streamwise pitches, and skew angles of each pair of trip strips were controlled by the optimization design variable set. The trailing edge coolant passage was cooled with pedestals that were shaped and positioned

for cooling purposes, as well as to provide increased stiffness against vibration. In this optimization, the relative dimensions of the pedestals were fixed.

The minimum and maximum bounds on the optimization design variables are given in Table 5. The turbulator heights and pitches were limited by the range of validity of their empirical correlations [19]. For example, the bounds on the turbulator heights were limited by the coolant passage height,  $H$ , between the suction and pressure sides, and the turbulator pitches were limited by a factor of turbulator heights,  $\epsilon$ . The bounds of the rib positions were set in order to produce a geometrically feasible design. In order to set the manufacturing constraints, the coolant passage walls were filleted, draft was included in the ribs, and the die pull angles,  $\theta_s$ , were constant along the span.

Table 5. Design variables of the P&W F100 second row high-pressure turbine blade optimization for increased cooling effectiveness.

Design Variable	Number in Set	Min.	Max.
Die pull angle, $\theta_s$	1 per rib (2)	$-10^\circ$	$65^\circ$
Rib position, $x_{rp}$	5 per rib (10)	variable	variable
Turbulator height, $\epsilon$	2 per cavity (4)	$0.04 * H$	$0.25 * H$
Turbulator pitch, $p$	2 per cavity (4)	$5 * \epsilon$	$70 * \epsilon$
Turbulator skew, $\alpha$	2 per cavity (4)	$0^\circ$	$90^\circ$
Total number	24		

The BEM analysis of temperature field was used in conjunction with the cooling effectiveness in order to develop the objective function,  $F$  (equation 13). The fully-coupled aero-thermo-fluid solution procedure was used to develop this function for each design perturbation while the constrained hybrid optimizer [5] maximized the cooling effectiveness objective (13). In serial processing mode, the entire optimization process utilized a full week of computing time on a Sun Ultra60 workstation. About 630 objective function analyses were required, resulting in approximately 1400 simulations of the temperature field using the BEM.

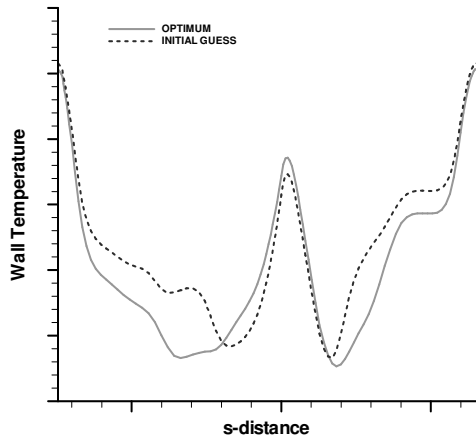


Figure 19: Comparison of external wall temperature predicted by the BEM at the midspan of the second HPT blade of the F100 engine: The optimization starting point is shown as a dashed line and the optimized design is shown as the solid line.

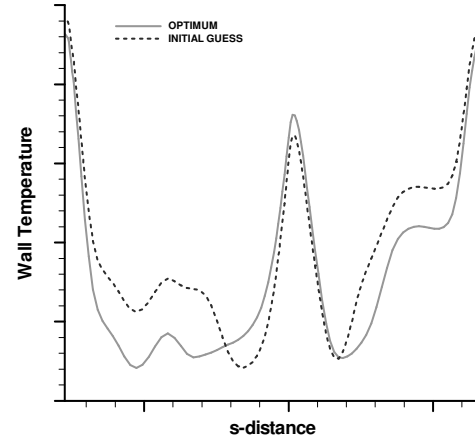


Figure 20: Comparison of external wall temperature predicted by BEM at the quarter-root span of the second HPT blade of the F100 engine. The optimization starting point is shown as a dashed line and the optimized design is shown as the solid line.

The optimization starting point, which was the production-version of the P&W F100 second turbine blade design, had an integrated average cooling effectiveness of 25.85 percent. The cooling effectiveness of the three-dimensional optimized design was 30.8 percent. Note that this cooling effectiveness was surface-area averaged over the entire external surface. There was little improvement in the wall temperature at the tip of the blade because the tip and turn surfaces were assumed to be adiabatic. The section-averaged cooling effectiveness of the root, quarter-root and mid-span sections demonstrated a more significant improvement.

Figures 19 and 20 show the external wall temperature variation predicted by the coupled aero-thermo-fluid analysis at the mid-span and quarter-root span. Note that the temperatures have been normalized in order to protect company proprietary information. The section-averaged wall temperatures were more than 25°K lower in the optimized design.

This was accomplished in several ways. Notice that the optimization algorithm reduced the internal ribbed turbulator heights near the root of the leading edge coolant passage (Fig. 21). That figure shows the history of the turbulator height design variables during the optimization run. Remember that the design variable set included four turbulator heights,  $\epsilon$ , two in each coolant passage, and in each coolant passage, one constant height from the root to about the 2/3 span, and the other from 2/3 span to the tip. The former are shown as filled symbols and the latter are shown as open symbols. The turbulator heights in the leading edge coolant passage (1) are circles and the midbody coolant passage (2) are squares.

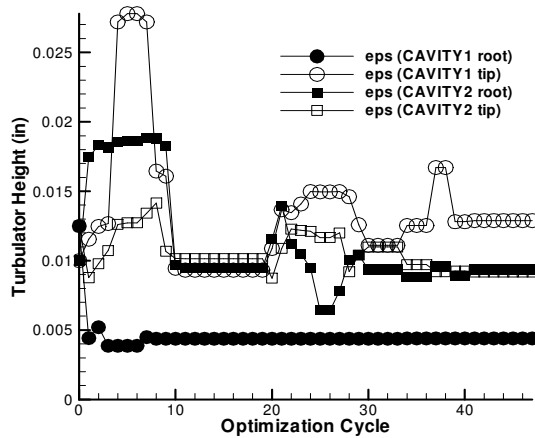


Figure 21: History of turbulator height design variables during cooling effectiveness optimization of F100 second turbine blade.

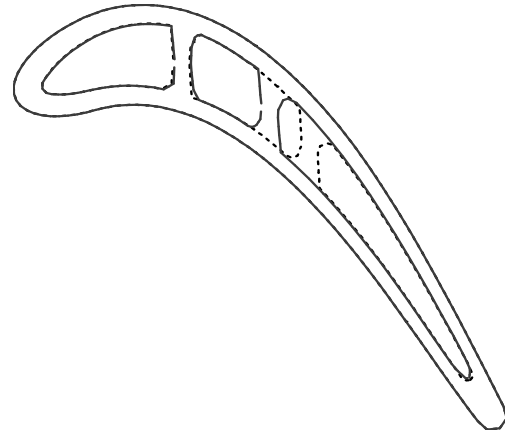


Figure 22: Comparison between the initial design (dashed lines) and final optimized design (solid line) is shown at the six design sections of Pratt & Whitney F100 second turbine blade.

The internal turbulator heights of the actual P&W F100 second blade design were relatively tall, but the optimization algorithm reduced them to their smallest allowable value as set by the lower design variable bound. That bound was set by the range of validity of the correlation in the internal coolant flow model. Notice that the optimization algorithm reduced the leading edge root values of  $\epsilon$  to its lower bound, and stayed on that lower bound, indicating that the optimizer was trying to remove that internal heat transfer enhancement. The reason for this is now clear. By removing the leading edge root turbulators, less heat will be absorbed by the blade so the coolant air would be cooler downstream. Unfortunately, the reduced internal heat transfer coefficients at the leading edge root had a penalizing effect.

The stagnation point at the leading edge of the blade was hotter in the optimized configuration, and this was more pronounced at the blade root. The optimization objective was a globally integrated function, so the localized heating at the leading edge had only a small

effect. This is interpreted as a problem with the integrated average cooling effectiveness objective function (equation 13). It would be more appropriate to more heavily weight the localized hot spots, particularly at the leading and trailing edges, to penalize optimization trends that cause them.

The 2-D section of the P&W F100 second turbine blade shown in Figure 22 has initial (production) geometry as dashed lines and the optimized geometry as solid lines. The optimization algorithm attempted to move the rib positions in order to do two things. First, the leading edge rib near the blade root was moved aft to produce a larger cross-sectional area in the leading edge coolant passage. This would allow for lower coolant Mach numbers at the trailing edge root. That effect was sought out because lower coolant speeds were correlated to lower heat transfer coefficients on the coolant passage walls, which would cause the coolant to absorb less heat. Second, the optimization algorithm moved the middle rib at the tip towards the leading edge to produce the opposite effect. The cross section clearly demonstrates a smaller cross-sectional area just after the first turn. In the fluid elements of the middle coolant passage near the tip, the internal flow Mach numbers increased from about 0.11 to 0.15. Combined with the increased turbulator height, the corresponding internal heat transfer coefficients were increased by about 45 percent. The optimization algorithm was favoring higher heat transfer coefficients in areas of the blade that were hotter, but it did this by sacrificing leading edge cooling.

The net effects of all of these design modifications were that the cooling effectiveness increased by 5 percent, while the coolant supply pressure remained the same, and the coolant mass flow rate was increased by only 0.5 percent. This increase is marginal when compared to the core engine flow rate, while the reduction in metal temperature by 25°K is substantial since it yields a doubling in the creep life of the blade at the P&W F100 engine operating conditions. The optimization algorithm found a design that achieved a 5 percent improvement in cooling effectiveness with only one-tenth more cooling air than what would normally be to achieve it. For example, if the design had remained fixed by assuming that the objective function  $F(V)$  in equation (14) stays the same, the same increase in the cooling effectiveness would require a 5 percent increase in the coolant flow rate.

Given the fact that the optimization starting point was the actual production version of the turbine blade that probably went through several manual design cycles, and considering that the optimization algorithm found an improved design that had more than a 25°K lower section-averaged metal temperature, this demonstration was successful at achieving the goals set to it, and the multi-disciplinary design and optimization methodology can be considered to be valid. This improvement in metal temperature would correlate to a factor of two improvements in creep life.

Further optimization of this turbine blade is also possible. The pedestal diameters and relative spacings could be included in the design variable set in an attempt to reduce the wall temperatures at the trailing edge. For a more accurate prediction of the temperature field in the trailing passage, the pedestals would need to be included in the thermal model (rather than just as a thermal boundary condition to a smooth coolant passage wall). There are also other possibilities. The external turbine blade shape could be modified in an effort to make the external aero-thermodynamics reduce the amount of heat absorbed by the blade. Each new design of the external airfoil would require a fully conjugate viscous three-dimensional steady-state CFD analysis of the hot gas flow field and the temperature field inside the blade [20]. This CFD solution would then be used to predict new external heat transfer coefficients, as well as provide an aerodynamic constraint function so that the efficiency and work of the turbine row could be fixed [21].

## 5. Design optimization and inverse design of alloys for turbine blades [22-24]

Alloy design for critical aero-engine components such as turbine blades and discs is a difficult, time-consuming and expensive process. The development period prior to application in an engine is typically of the order of ten years. Airframe manufacturers usually announce a new design only five years prior to flight certification. This leaves the engine designers only half the current period necessary for materials development.

Indirect Optimization based upon Self-Organization (IOSO) algorithm [9] was used in conjunction with experimental evaluations of maximum strength and time-to-rupture at high temperature to maximize these two properties in nickel based steel alloys [22,23]. This provides the first realistic demonstration of the entire alloy design optimization procedure and simultaneous experimental verification of this procedure. We started by using 120 experimentally tested nickel based alloys and optimized concentrations of six alloying elements in order to predict 20 new alloy compositions with potentially better properties. After experimentally testing these 20 new alloys, it was found that 7 of them indeed had superior strength and time-to-rupture at high temperature as compared to the original 120 alloys. The IOSO optimization procedure was repeated a total of four times whereby 20 new alloys were predicted and experimentally tested during each of the four design iteration cycles. The properties of the newly found alloys consistently continued improving from one iteration to the next. This was confirmed by experimentally evaluating these new alloys. This alloy design methodology is applicable to arbitrary alloys. It does not require any mathematical modeling of the physical properties since they are determined experimentally. This assures the reliability of this approach to alloy design and makes it affordable since it requires a relatively small number of new alloys to be manufactured and experimentally tested.

Specifically, this work was aimed at optimizing nickel based heat-resistant alloy castings containing *Ni, C, Cr, Co, W, Mo, Al, Ti, B, Nb, Ce, Zr, Y*, and trace amounts of *S, P, Fe, Mn, Si, Pb, Bi*. Thermal treatment of the samples involved heating them to 1210 C, holding for 4 hours, and air cooling. During the tests the stress at room temperature ( $\sigma$ ) and the time to survive until rupture at temperature of 975 C and stress of 230 N/mm<sup>2</sup> were measured. The technology used in the casting allowed us to alter the chemical composition by varying concentrations of the following elements: *Ni, C, Cr, Co, W, Mo, Al, Ti*. The concentrations of *Nb, B, Ce, Zr, Y* in all test samples were 1.1%, 0.025%, 0.015%, 0.04%, and 0.01%, respectively. Average concentrations of trace alloying elements were: S (0.0037%), P (0.006%), Fe (0.085%), Mn (0.013%), Si (0.067%), Pb (0.0005%), Bi (0.0005%). In this task the concentrations of seven elements: *C, Cr, Co, W, Mo, Al, Ti* were used as variables..

The percent of nickel represented the remaining amount of the alloying mixture. User-specified minimum and maximum allowable values of the seven alloying elements are presented in Table 6.

Table 6. Prescribed ranges of optimization variables

Element	Minimum %	Maximum %
C	0.13	0.20
Cr	8.0	9.5
Co	9.0	10.5
W	9.5	11.0
Mo	1.2	2.4
Al	5.1	6.0
Ti	2.0	2.9

The optimization was conducted by simultaneously maximizing stress (SIGMA) and time-to rupture (HOURS). At each optimization iteration, a two-criterion optimization task with a specified number of Pareto optimal points was solved. The user-specified number of Pareto points was 20.

The total number of experimentally evaluated alloy samples during the solution of this particular optimization problem was specified by the user to be 200. At the start, the initial experiment plan including 120 points was developed by distributing their chemical compositions via Sobol's algorithm<sup>14</sup>. This information was used for building an approximation function (a multi-dimensional response surface) for the first iteration. This approximation function was optimized using IOSO. The result was a set of chemical compositions of 20 new alloys which could be a part of the current Pareto set (Fig. 23).

Next step was manufacturing and experimental evaluation of the two properties (maximum stress and time-to-rupture at 975 C) for each of these 20 newly found alloys.

Then, we defined a Pareto set using all ( $120 + 20 = 140$ ) experimental points. This research shows that only seven out of 20 newly found alloys belong to the current Pareto set after the first iteration. This means that all triangles in Fig. 23 are real-life materials with new chemical compositions, but only 7 of them belong to the current Pareto set because these chemical compositions can improve both optimization objectives for real-life materials. The remaining 13 newly found alloys are not the best as revealed by the experimental research, because these alloys do not belong to the current Pareto set after the first iteration for real-life material. This is why we named these 13 alloys as "points with bad predictive properties" (Fig. 23). But, these 13 new alloys bring some new information about topology of the objectives. That is why we can now build a new approximation function (response surface) with a higher level of accuracy.

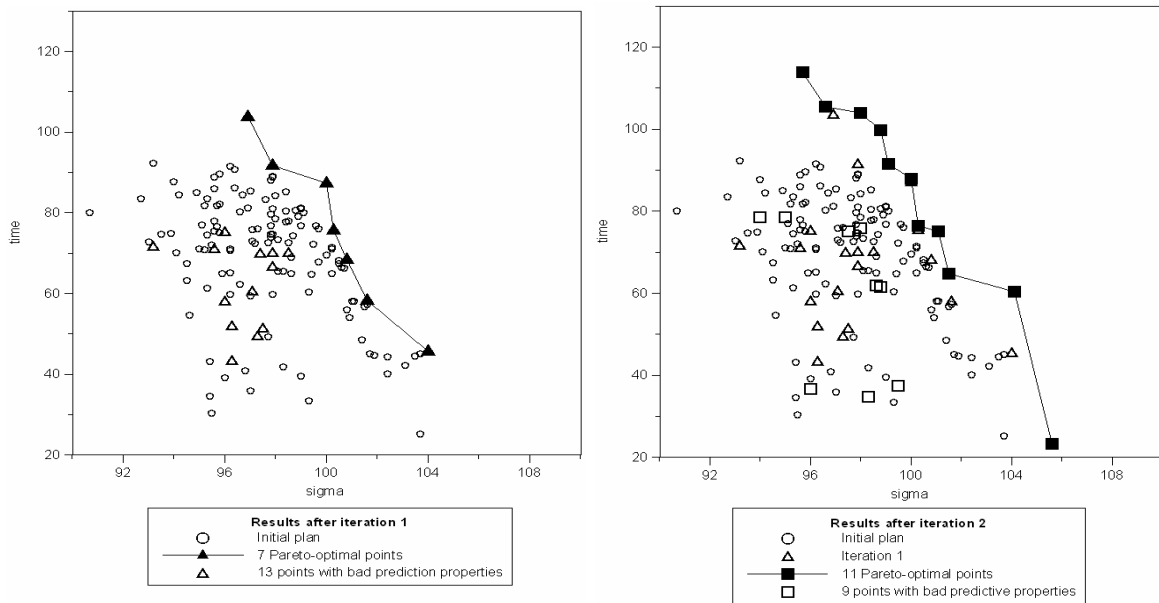


Figure 23: Initial 120 alloys plus 20 alloys from first iteration (left) and 20 alloys predicted by the 2<sup>nd</sup> iteration (right) with IOSO optimizer. All were then experimentally tested for maximum strength and time-to-rupture at 975 degrees Celsius.

Second iteration followed the same procedure, but now we used all 140 experimentally evaluated alloys (7 of them were in the current Pareto set after the first iteration). Third iteration used 160 alloys and fourth iteration used 180 alloys (Fig. 24).

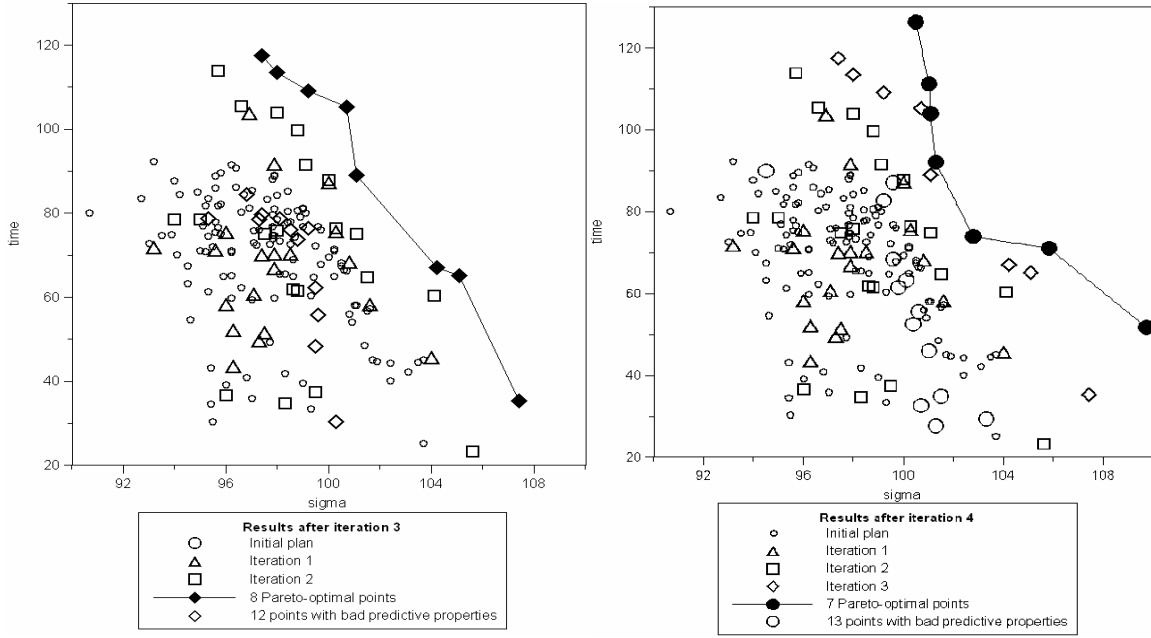


Figure 24: Initial 120 alloys plus 20 alloys from first iteration, 20 alloys from 2<sup>nd</sup> iteration 20 alloys from third iteration (left) plus 20 alloys predicted by fourth iteration (right) with IOSO optimizer. All of these alloys were experimentally tested for maximum strength and time-to-rupture at 975 degrees Celsius.

It should be pointed out that the presented work represents an automatic search for concentrations of alloying elements that will simultaneously provide extreme values of several objectives. This is a different concept from an inverse determination of chemical concentrations of alloying elements that will create alloys which satisfy prescribed values of multiple physical properties.

The inverse problem in design of alloys is determination of chemical composition(s) of alloy(s) that will provide specified levels of, for example, stress at a specified temperature for the specified length of time. The inverse problem can be then formulated as, for example, a multi-objective optimization problem with a given set of equality constraints [24].

For example, this formulation allows a structural design engineer who designed a machine part to ask a materials scientist to provide a precise chemical composition of an alloy that will sustain a specified stress level, at a specified temperature, and last until rupture for a specified length of time. This inverse method uses a variant of Prof. Yegorov-Egorov's optimization algorithm known as IOSO [9] to determine not one, but a number of alloys (Pareto front points) each of which will satisfy the specified properties while having different percentages of each of the alloying elements (a different "recipe"). This provides the user of the alloy with increased flexibility when deciding to create such an alloy, because he/she can use the "recipe" which is made of the most readily available and the most inexpensive elements on the market at that point in time.

In particular, the objective was to determine chemical composition(s) of high temperature steel alloys that will have specified (desired) physical properties. Design variables were concentrations (percentages) of each of the following 14 alloying elements *C, S, P, Cr, Ni, Mn, Si, Mo, Co, Nb, W, Sn, Zn, Ti*

No mathematical analysis was used to evaluate the objectives. The evaluations were performed using classical experiments on candidate alloys. In other words, we used an existing experimental database. Optimization criteria was formulated as a multi-objective statement with three simultaneous objectives: minimize the difference between the specified



and the actual stress, minimize the difference between the specified and actual maximum temperature, and minimize the difference between the specified and actual time to rupture

The results of this multiple simultaneous least-square constrained minimization problem cannot be visualized for more that two alloying species at a time. For example, when concentrations of only two alloying elements like Ni and Cr are visualized, and temperature and life expectancy are unconstrained (unspecified) the optimizer will give a fairly large domain for possible variations of the concentrations of Cr and Ni. But, as the constraints on temperature level are introduced and progressively increased, the feasible domain for varying Cr and Ni will start to shrink (Fig. 25). Similar general trend can be observed when the life expectancy is specified and progressively increased (Fig. 26)..

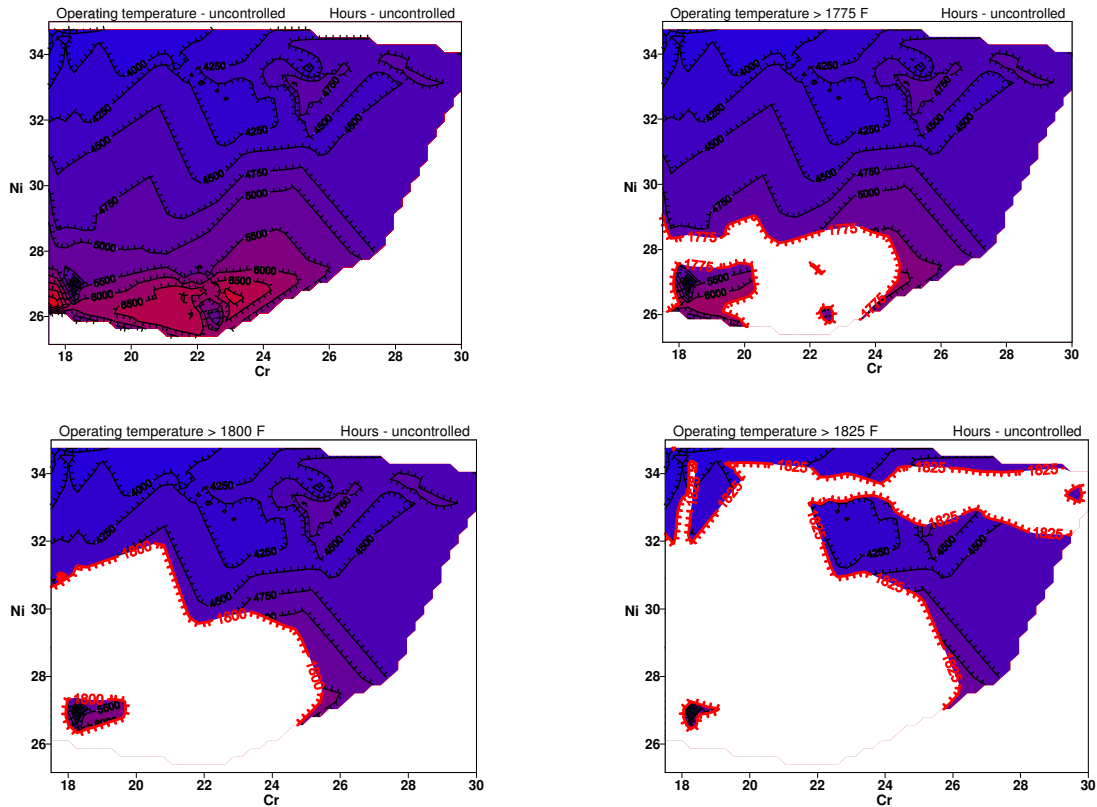
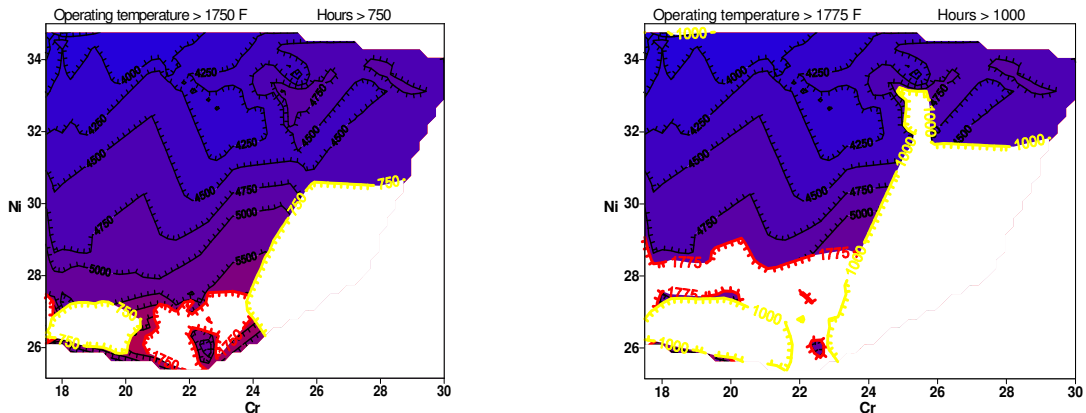


Figure 24: Effect of increasing the temperature [24].



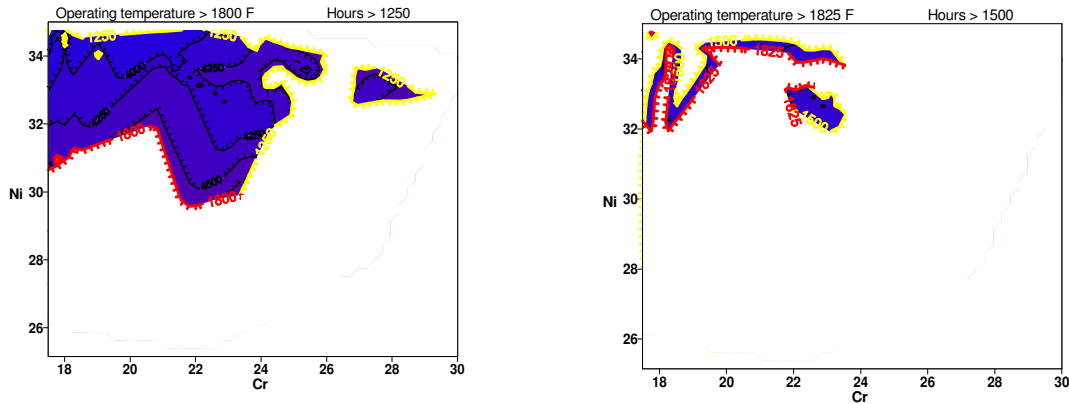


Figure 25: Effect of increasing the time-to-rupture requirement [24].

Additional objectives can also be simultaneously considered so that the alloys could be optimized also for the minimum cost, minimum weight, etc.

## References

- [1] Martin, T. J. and Dulikravich, G. S., "Aero-Thermo-Elastic Concurrent Design Optimization of Internally Cooled Turbine Blades," a chapter in *Coupled Field Problems, Series on Advances in Boundary Elements* (eds: Kassab, A. J. and Aliabadi, M. H.), WIT Press, Boston, MA, 2001, pp. 137-184.
- [2] Martin, T. J. and Dulikravich, G. S., "Aero-Thermal Analysis and Optimization of Internally Cooled Turbine Blades," *XIII International Symposium on Air-breathing Engines (XIII ISABE)*, Chattanooga, TN, Sept. 8-12, 1997, ISABE 97-7165, Volume 2, 1997, pp. 1232-1250.
- [3] Martin, T. J., Dulikravich, G. S., Han, Z.-X. and Dennis, B. H., "Minimization of Coolant Mass Flow Rate in Internally Cooled Gas Turbine Blades," *ASME paper 99-GT-146*, International Gas Turbine & Aeroengine Congress & Exposition, Indianapolis, IN, June 7-10, 1999.
- [4] Martin, T. J. and Dulikravich, G. S., "Analysis and Multi-disciplinary Optimization of Internal Coolant Networks in Turbine Blades", *AIAA Journal of Propulsion and Power*, vol. 18, no. 4, 2002, pp. 896-906.
- [5] Dulikravich, G. S., Martin, T. J., Dennis, B. H. and Foster, N. F., "Multidisciplinary Hybrid Constrained GA Optimization", a chapter in *EUROGEN '99 - Evolutionary Algorithms in Engineering and Computer Science: Recent Advances and Industrial Applications*, (eds K. Miettinen, M. M. Makela, P. Neittaanmaki and J. Periaux), John Wiley & Sons, Ltd., Jyväskylä, Finland, May 30 - June 3, 1999, pp. 231-260.
- [6] Dennis, B. H., Egorov, I. N., Dulikravich, G. S. and Yoshimura, S., "Optimization of a Large Number of Coolant Passages Located Close to the Surface of a Turbine Blade", *ASME paper GT2003-38051*, ASME Turbo Expo 2003, Atlanta, GA, June 16-19, 2003.
- [7] Han, Z.-X., Dennis, B. H. and Dulikravich, G. S., "Simultaneous Prediction of External Flow-Field and Temperature in Internally Cooled 3-D Turbine Blade Material," *Internat. J. of Turbo & Jet-Engines*, Vol. 18, No. 1, 2001, pp. 47-58.
- [8] Goldberg, D. E. *Genetic Algorithms in Search, Optimization and Machine Learning*, Addison-Wesley, 1989.
- [9] Egorov, I. N., Kretinin, G. V., Leshchenko, I. A. and Kuptzov, S. V., "Multi-objective robust design optimization using IOSO technology algorithms", a chapter in *Evolutionary Algorithms and Intelligent Tools in Engineering Optimization* (eds: W.

- Annicchiarico, J. Périaux, M. Cerrolaza and G. Winter), CIMNE, Barcelona, Spain 2004.
- [10] Pritchard, L. J., "An Eleven Parameter Axial Turbine Airfoil Geometry Model, ASME paper 85-GT-219, 1985.
  - [11] Sobieczky, H., Dulikravich, G. S. and Dennis, B. H., "Parameterized Geometry Formulation for Inverse Design and Optimization," 4<sup>th</sup> International Conference on Inverse Problems in Engineering: Theory and Practice (4icipe), (ed: Orlande, H. R. B.), Angra dos Reis, Brazil, May 26-31, 2002.
  - [12] Dennis, B. H., Egorov, I. N., Sobieczky, H., Dulikravich, G. S. and Yoshimura, S., "Parallel Thermoelasticity Optimization of 3-D Serpentine Cooling Passages in Turbine Blades", *International Journal of Turbo & Jet-Engines*, vol. 21, no. 1, 2004, pp. 57-68.
  - [13] ADVENTURE Project Homepage, <http://adventure.q.t.u-tokyo.ac.jp>.
  - [14] Gropp, W., Lusk, E., and Skjellum, A., 1994, *Using MPI: Portable Parallel Programming with the Message-Passing Interface*, MIT Press.
  - [15] Larson, F. R. and Miller, J., "A Time Temperature Relationship for Rupture and Creep Stresses," *ASME Journal*, vol. 74, 1952, pp. 705.
  - [16] Menon, M. N., "A Model for Primary, Secondary and Tertiary Creep Rates," *Proc. of the 5th Internat. Conf. on Creep of Materials*, Lake Buena Vista, FL, May 18-21, 1992.
  - [17] Lakshminarayana, B., *Fluid Dynamics and Heat Transfer of Turbomachinery*, John Wiley & Sons Inc., N.Y., 1996.
  - [18] Press, W. H, Teukolsky, S. A., Vetterling, W. T. and Flannery, B. P., *Numerical Recipes in FORTRAN, The Art of Scientific Computing, 2nd Edition*, Cambridge University Press, Cambridge, UK, 1986.
  - [19] Mochizuki, S., Takamura, J., Yamawaki, S., and Yang, W. J., "Heat Transfer in Serpentine Flow Passages With Rotation," *ASME J. of Turbomachinery*, vol. 116, 1994, pp. 133-140.
  - [20] Han, Z.-X., Dennis, B. H. and Dulikravich, G. S., "Simultaneous Prediction of External Flow-Field and Temperature in Internally Cooled 3-D Turbine Blade Material," *International J. of Turbo & Jet-Engines*, Vol. 18, No. 1, 2001, pp. 47-58.
  - [21] Dennis, B. H., Dulikravich, G. S. and Han, Z.-X., "Constrained Optimization of Turbomachinery Airfoil Shapes Using a Navier-Stokes Solver and a Genetic/SQP Algorithm," *AIAA J. of Propulsion and Power*, Vol. 17, No. 5, 2001, pp. 1123-1128.
  - [22] Dulikravich, G. S., Egorov, I. N., Sikka, V. N. and Muralidharan, G., "Semi-stochastic optimization of chemical composition of high-temperature austenitic steels for desired mechanical properties", 2003 TMS Annual Meeting, Yazawa International Symposium: Processing and Technologies, TMS Publication; Kongoli, F., Itakagi, K., Yamaguchi, C., Sohn, H.-Y., Eds.; Vol. 1, pp. 801-814, San Diego, CA, March 2-6, 2003.
  - [23] Yegorov-Egorov, I. N. and Dulikravich, G. S., "IOSO optimization of steel alloy chemical composition for maximum stress and time-to-rupture at high temperature", paper AIAA-2004-4348, 10<sup>th</sup> AIAA/ISSMO Multidisciplinary Analysis and Optimization Conference; Messac, A., Renaud, J., Eds.; Albany, NY, Aug. 30 – Sept. 1, 2004.
  - [24] Yegorov-Egorov, I. N. and Dulikravich, G. S., "Inverse design of alloys for specified stress, temperature and time-to-rupture by using stochastic optimization", International Symposium on Inverse Problems, Design and Optimization – IPDO, eds., Orlande, H. R. B. and Colaco, M. J., Rio de Janeiro, Brazil, March 17-19, 2004.